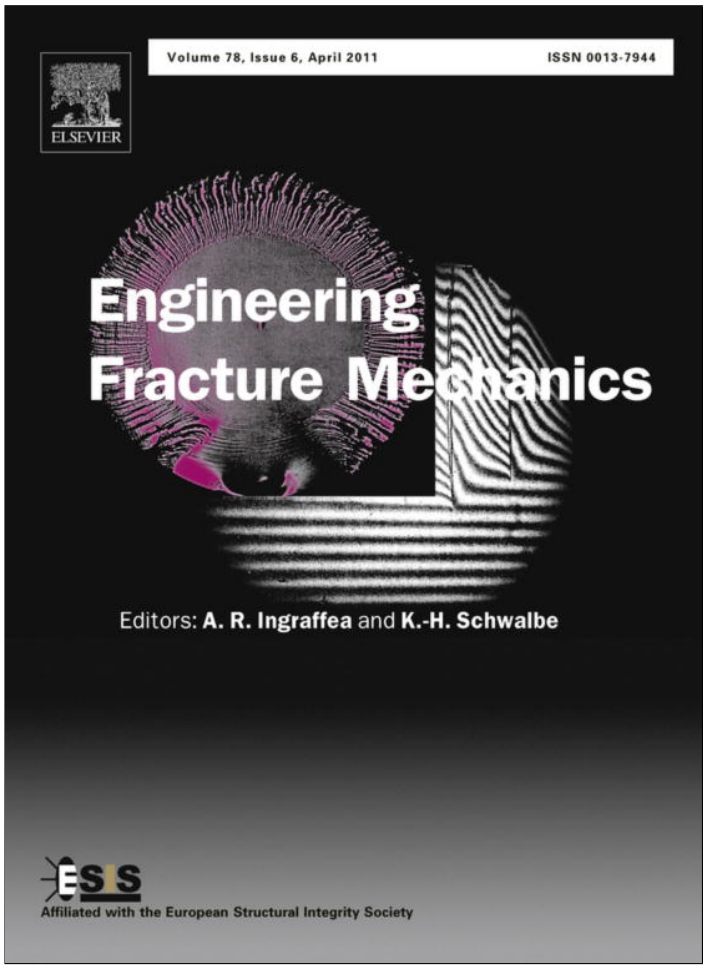

Engineering Fracture Mechanics 78 (2011) 1289–1305

Contents lists available at ScienceDirect

Engineering Fracture Mechanics

journal homepage: www.elsevier.com/locate/engfracmech

An experimental investigation of dynamic crack growth past a stiff inclusion

K.C. Jajam, H.V. Tippur *

Department of Mechanical Engineering, Auburn University, Auburn, AL 36849, USA

ARTICLE INFO

Article history:
Received 15 August 2010
Received in revised form 24 January 2011
Accepted 6 February 2011
Available online 12 February 2011

Keywords:
Optical metrology
Crack–inclusion interaction
Dynamic fracture
Digital image correlation
High-speed imaging
Adhesion strength
Surface roughness

ABSTRACT

The mechanics of transient crack growth past stiff inclusions embedded in a relatively compliant matrix are studied optically under stress wave dominant loading conditions. An ultra high-speed rotating mirror-type CCD digital camera is used to record gray scales in the crack–inclusion vicinity at rates of up to 300,000 frames per second and 1000 × 1000 pixel resolution in real time. By analyzing the images before and after deformations, crack-tip deformation histories from the time of impact up to complete fracture are mapped and fracture parameters are extracted. The effects of inclusion–matrix adhesion strengths (weak and strong) and eccentricity of the inclusion relative to the crack path in the crack-tip vicinity are examined. A weakly bonded inclusion attracts and traps a dynamically growing mode-I crack momentarily whereas the same is deflected away by the inclusion if it is bonded strongly to the matrix. As a result, significantly higher re-initiation crack velocities are seen in weakly bonded inclusion cases upon re-initiation when compared to the strongly bonded counterparts. The effective stress intensity factor histories extracted from measured full-field displacements show a spike in values corresponding to higher crack velocities. Further, crack-tip mode-mixities correlate well with crack attraction and deflection mechanisms. The measured surface roughness is found to be consistently higher for weakly bonded inclusion specimens compared to the strongly bonded ones.

1. Introduction

Multiphase materials made of constituents with synergistic characteristics are in demand for use in a wide variety of engineering applications. Introduction of second phase fillers and alteration of filler–matrix adhesion characteristics offer a cost effective way of functionalizing a polymer. It further allows optimization of material performance in terms of physical, thermo-mechanical and dielectric attributes. Effective stiffness, strength and fracture toughness of the resulting material system can be tailored using stiff or compliant fillers relative to the matrix. However, the presence of cracks in any of the phases influences the overall mechanical properties in general and fracture behavior in particular. The filler–matrix interfaces, being planes of low or high strength, also play a vital role in attracting or deflecting a crack away. Accordingly, understanding the failure behavior of such materials under stress-wave loading conditions is essential for assessing mechanical integrity under dynamic conditions. Some knowledge can be gained on this topic by studying interactions between a dynamically propagating crack and an isolated stiff inclusion as a function of the inclusion–matrix interfacial strength and the inclusion location relative to the crack-tip.

At the moment, studies on dynamic failure behavior of heterogeneous materials have mostly been carried out under quasi-static loading conditions. Further, most reported studies are analytical and/or numerical in nature and rather limited

* Corresponding author. Tel.: +1 334 844 3327; fax: +1 334 844 3307.
E-mail address: htippur@eng.auburn.edu (H.V. Tippur).

0013-7944/$ - see front matter © 2011 Elsevier Ltd. All rights reserved.
doi:10.1016/j.engfracmech.2011.02.005

understanding from an experimental perspective exists. Early analytical study by Tamate [1] focused on complex potentials to analyze stress fields and stress intensity factors for mode-I cracks due to interactions between a compliant matrix crack and a stiff circular inclusion and *vice versa*. Evans [2] reported the effect inclusions have on the fracture of ceramics by evaluating the local stresses around inclusions due to thermal expansion and elastic modulus mismatch and calculated approximate magnitude of stress intensity factors at interface cracks. Erdogan et al. [3] developed expressions for mode-I and mode-II stress intensity factors by using asymptotic values of density functions of integral equations in terms of crack face displacements for interactions between a circular inclusion and an arbitrarily oriented crack. Bush [4] used boundary element method to model interactions of a matrix crack with a single inclusion and a cluster-of-inclusions in order to study crack trajectories and crack driving forces for weakly and strongly bonded inclusion–matrix interfaces. Symmetric-Galerkin boundary element method was adopted by Kitey et al. [5] to simulate two dimensional mixed-mode quasi-static crack growth near strongly bonded stiff particle clusters. They observed differences in crack trajectories with respect to the cluster orientation and concluded that the crack driving force is affected much earlier than the perceivable crack deflection and energy release rate increases with increase in the inclusion eccentricity relative to the crack. Li and Chudnovsky [6,7] examined the effects of an elastic inclusion on the energy release rate for crack extension and showed that the crack-tip is shielded from far field stresses when it approaches a rigid inclusion and stresses get amplified when it propagates past the inclusion. More recently, a theoretical model based on the application of a coupled stress and energy criterion for the prediction of the crack onset at the interface between a stiff cylindrical inclusion and a compliant unbounded matrix subjected to a remote uniaxial transverse tension is developed by Mantic [8].

Although information in terms of analytical and numerical perspectives can be noted from previous reports, experiments are still lacking. Among the few experimental investigations on this topic, O'Toole and Santare [9] studied crack–inclusion interactions by bonding two identical elliptical steel inclusions on the two faces of a cracked thin polymer plate. Li and Chudnovsky [10] realized perfectly bonded second phase circular inclusion by introducing stiff and compliant circular inclusion in photodegradable plastic material specimens by selectively irradiating with ultraviolet radiation. They studied fatigue crack growth behavior and analyzed fracture surface morphology qualitatively. Savalia and Tippur [11] carried out an experimental–numerical study of crack–inclusion interactions under quasi-static loading conditions using moiré interferometry and finite element analysis. As noted earlier, most of the experimental studies on this topic found in the literature are limited to quasi-static loading conditions with the exception of the one reported by Kitey and Tippur [12]. They have investigated the dynamic crack growth behavior in the vicinity of an isolated stiff inclusion using the method of reflection mode Coherent Gradient Sensing (CGS). Being a surface slope detection method, CGS interferograms heavily localized near the regions of stress concentration and could not be analyzed satisfactorily when the crack-tip was in the inclusion vicinity. The present work essentially builds on the work of Kitey and Tippur and extends their observations by directly measuring more readily interpretable full-field surface displacement components both before and after crack–inclusion interaction with an eventual goal of evaluating field quantities in the matrix as well as the inclusion. Moreover, they have extracted stress intensity factors (SIF) using governing equations for a monolithic material and the SIF values at the crack–inclusion interface are questionable and need to be analyzed using bimaterial field equations, as well as some evidence of experimental repeatability is also required for this kind of study.

The experimental techniques for evaluating fracture parameters in real time in a dynamic failure event involving crack initiation and propagation were somewhat limited to several full-field optical methods such as photoelasticity, optical caustics, CGS, and moiré interferometry. All interferometric techniques have stringent surface preparation requirements such as preparation of birefringent coatings in reflection photoelasticity, transfer of gratings in moiré interferometry and preparation of specularly reflective surface for CGS. However, recent progress in image processing methods, high-speed computations and the advent of ultra high-speed digital photography with relatively high spatial and temporal resolutions have made it possible to use digital image correlation (DIC) [13–18] method. Recently, Tippur and his coworkers [19–21] have fashioned this method for measuring in-plane displacements under stress-wave loading conditions using high-speed digital cameras. This method offers the convenience of minimum surface preparation and is optically less demanding. These aspects have also motivated adopting the method of 2D digital speckle correlation in conjunction with an ultra high-speed digital camera to carry out an investigation of the mechanics of interactions between a dynamically growing matrix crack and a stiff cylindrical inclusion as a function of inclusion–matrix interfacial strength and the inclusion location.

In the ensuing sections, the basic concept and the approach of the optical methodology employed in this study are briefly described. Next, the details of specimen preparation and geometry followed by experimental setup and testing procedure are provided. This is followed by a description of experimental observations and results in terms of contours of displacements and various fracture parameters such as crack velocity histories, effective stress intensity factor histories, mode-mixity behaviors. The results are supported by examining fractured surfaces and roughness measurements. Finally, the major conclusions of the current study are discussed and summarized.

2. Experimental approach

In the present study, decorated random speckle patterns on a specimen surface were acquired during a dynamic fracture event. The light intensity of these images was recorded at two different states, one before and another after deformation. The corresponding individual images from deformed and undeformed sets were paired and each pair was analyzed separately.

That is, a sub-image in an undeformed image was chosen and its location in the corresponding deformed image was identified. Once the location of a sub-image in the deformed image was found, the local displacements of the sub-image could be determined. In this study, an approach[1] developed by Tippur and his coworkers [19,20] on a MATLAB™ platform, was used to estimate in-plane (2D) surface displacement components. In the first step, displacements were estimated by performing a 2D cross-correlation operation of gray scales in the Fourier domain and the peak of the correlation function detected to a sub-pixel accuracy using bicubic interpolation. This process was repeated for the entire image to obtain full-field in-plane displacements. In the second step, an iterative approach based on nonlinear least-square minimization was used to minimize the 2D cross-correlation function in the spatial domain in order to refine the displacement fields obtained in the previous step. Additional details regarding image acquisition and analysis are reported in the following sections. Other details regarding camera calibration can be found in the earlier publications.

3. Experimental details

3.1. Specimen preparation and geometry

Edge cracked epoxy specimens were prepared by mixing a low viscosity Bisphenol-A resin and an amine-based hardener (Epo-Thin™ from Beuhler, Inc. USA) in the ratio of 100:39, as the matrix material. Before pouring the mixture into the mold, a cylindrical glass inclusion of diameter d = 4 mm and length equal to the specimen thickness (8.6 mm) was positioned at the center of the mold as shown in Fig. 1a. To avoid residual stresses, the material was cured slowly at room temperature. A weak inclusion–matrix interface was created by wiping the inclusion with a thin layer of grease whereas a strong adhesion was achieved by treating the inclusion with amine-based silane coating (γ-aminopropyltrimethoxysilane). The cured sheets were then machined into test specimens of dimensions 206 mm $\times$ 50 mm $\times$ 8.6 mm. An edge notch of 5 mm in length was cut using a high-speed diamond impregnated circular blade (thickness $\sim$300 μm) and then the notch tip was sharpened using a razor blade in order to have a sharp crack-tip to achieve a relatively quiescent crack initiation followed by a steady growth. A magnified view of the sharpened crack-tip is shown in Fig. 1b and c with front- and back-side views of the specimen respectively.

A random speckle pattern was created on the surface of the sample by spraying a fine mist of black and white paints alternatively. Fig. 1d depicts the specimen geometry, dimensions and loading configurations with an illustration of random speckle pattern on it. The region in the dotted box represents 30 $\times$ 30 mm^2 region of interest containing the embedded cylindrical glass inclusion. The line joining the impact point to the crack-tip represents the line-of-symmetry. The location of the inclusion with respect to the initial crack-tip is defined as eccentricity, e, which is the distance between the inclusion center and the line-of-symmetry. In this work, the inclusion was located at two different eccentricities, e = 0 and 3d/4, being referred as symmetric and eccentric (or asymmetric) cases respectively (Fig. 2). In both cases, the inclusion was positioned at a constant distance of 20 mm from the bottom edge of the specimen containing the initial notch.

3.2. Experimental setup and testing procedure

A schematic of the dynamic experimental setup employed in this work is shown in Fig. 3. The setup included a drop tower (Instron-Dynatup 9250HV) for impacting the specimen and an ultra high-speed digital framing camera (Cordin-550) for capturing speckle images in real-time. The drop tower was equipped with an instrumented tup and a pair of anvils for recording force and support reaction histories respectively. The setup also included a delay/pulse generator to trigger the camera when the impactor contacted the specimen. Since the images were acquired during the dynamic event, lasting about 180 μs, two high-energy flash lamps, triggered by the camera, were employed to illuminate the sample surface. Two separate computers, one to record the impact force and anvil reaction histories, and the other to control the high-speed camera and to store the images at desired framing rates were utilized. The reflected light intensity from specimen surface in the region of interest where surface deformations take place was recorded.

The ultra high-speed digital framing camera is equipped with a combination of CCD based imaging technology and a high-speed rotating mirror optical system (see Fig. 4.). It is capable of recording images at rates of up to 2 million frames per second on 32 individual 1000 $\times$ 1000 pixel CCD image sensors positioned circumferentially around a five-facet rotating mirror which reflects and sweeps light over these sensors. Details about the camera performance evaluation and optical calibration can be found in Refs. [19,20]. The specimen decorated with random speckles was initially rested on two instrumented anvils and the camera was focused on a 30 $\times$ 30 mm^2 region of interest on the specimen in the vicinity of crack-tip and inclusion. Prior to impacting the specimen, a set of 32 images were recorded at a framing rate of 300,000 frames per second and stored. While maintaining all camera settings same, another set of 32 images was captured when the specimen was impacted at a velocity of 4.5 m/s. A total of 32 images were recorded with a 3.33 μs interval between successive images for each undeformed and deformed sets. The corresponding two images for each sensor were paired from undeformed and deformed sets and each of these 32 matched pairs was analyzed individually.

[1] Unlike in the earlier works [19–21], the third smoothing step was avoided since stress intensity factors were estimated directly from in-plane displacement components.

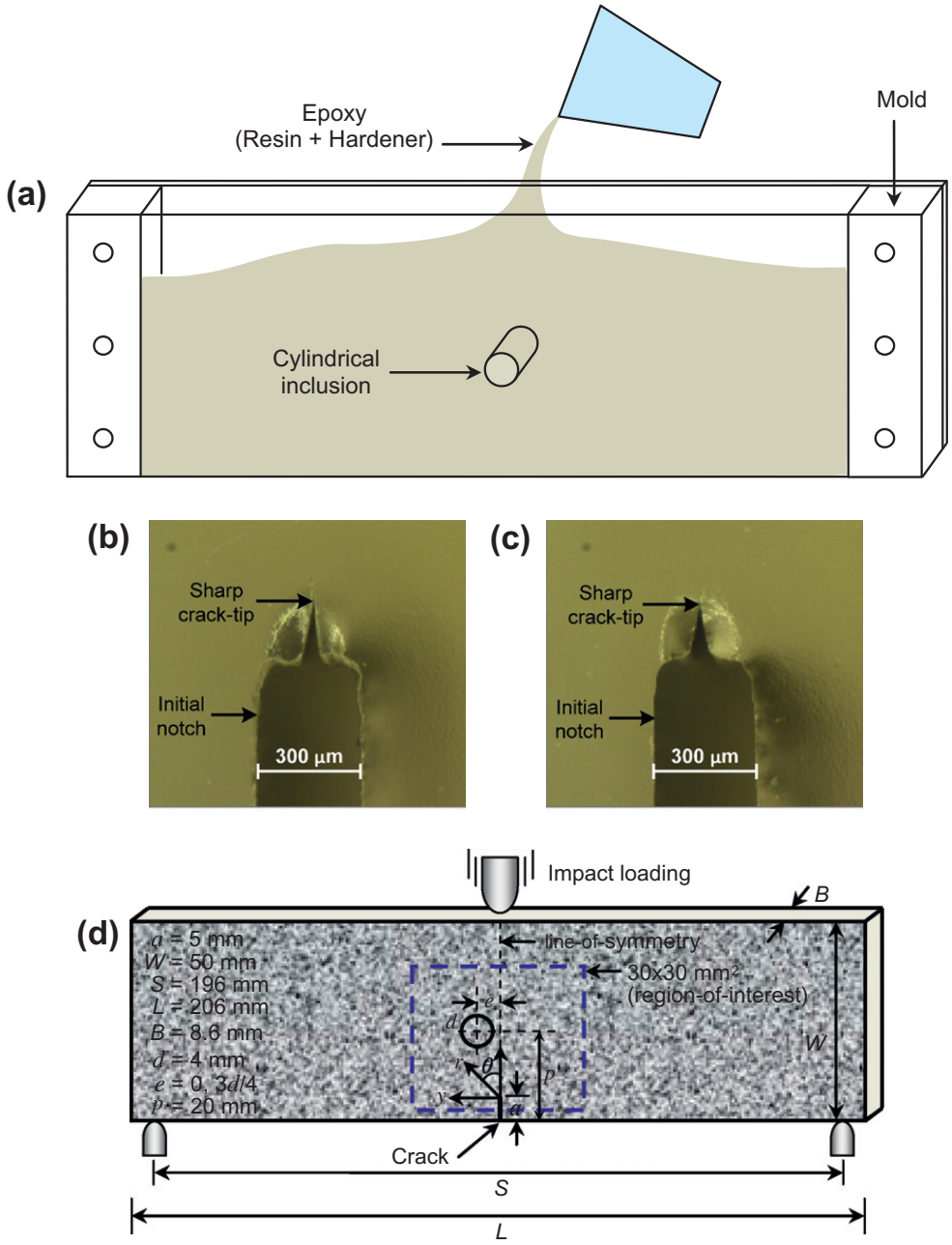

Fig. 1. Specimen details: (a) Sample preparation. (b) Sharp crack-tip: front-side view of the specimen. (c) Sharp crack-tip: back-side view of the specimen. (d) Specimen geometry and loading configuration with crack-tip coordinate system and inclusion location, with an illustration of random speckle pattern.

3.3. Image analysis details

As noted earlier, the recorded images corresponded to a 30×30 mm^2 region on the specimen surface. The size of the decorated speckles and the optical magnification used were such that each speckle occupied 4–6 pixels on the image plane. Care was also exercised regarding electronic gain setting of the high-speed camera sensors and illumination intensity of the flash lamps to produce an approximately Gaussian distribution of gray scales for each image in the mid-range of 0–255 (8 bit) intensity range. That is, any possible saturation or underexposure of pixels was avoided by trial and error before carrying out the actual experiment. Each resulting image was segmented into sub-images consisting of 24×24 pixels for analysis. No overlapping of sub-images was adopted during image correlation operations in either of the steps described earlier. This resulted in 40×40 matrix of data points in the region of interest for each displacement field.

3.4. Evaluation of crack velocity and stress intensity factors

The position of current crack-tip from each digitized image was used to measure the instantaneous values of crack length. The crack velocity (c) was then evaluated from crack length histories using the central difference method,

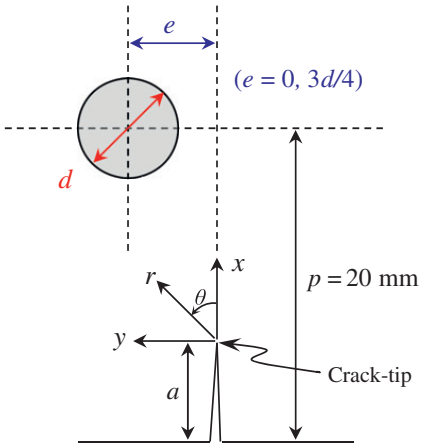

Fig. 2. The inclusion location relative to the initial crack-tip: symmetrically located inclusion ($e = 0$) and eccentric inclusion ($e = 3d/4$).

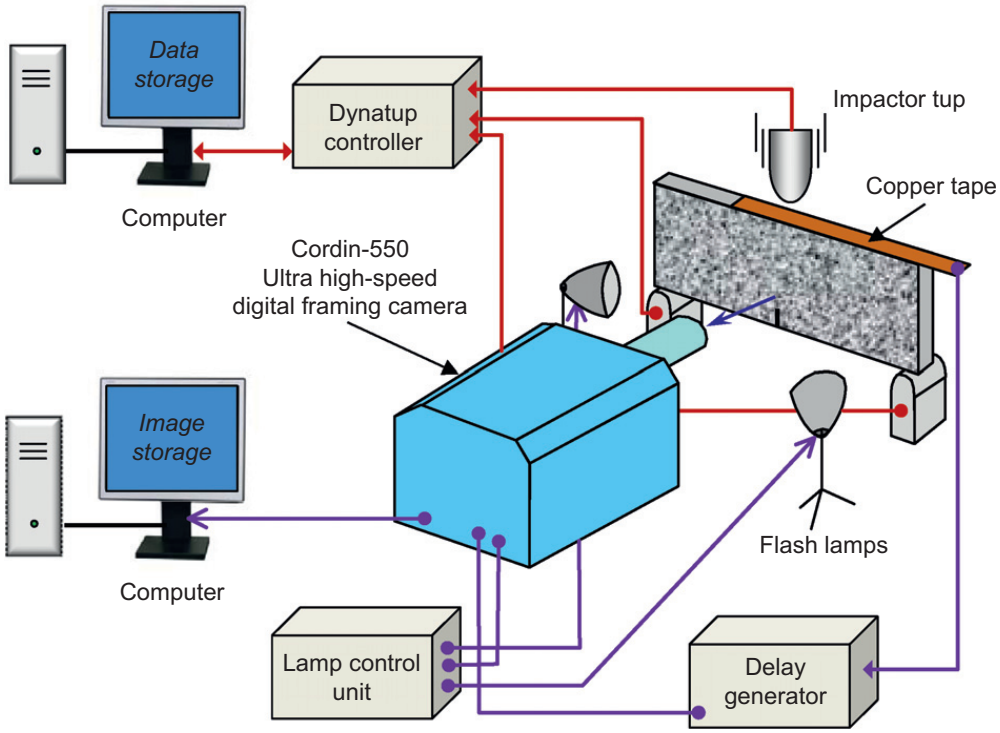

Fig. 3. Schematic of the dynamic experimental setup.

$$c_i = \left(\frac{da}{dt}\right)_i = \frac{a_{i+1} - a_{i-1}}{t_{i+1} - t_{i-1}} \tag{1}$$

where a and t are crack length and time respectively at a given instant i.

The mode-I and mode-II stress intensity factors (SIFs) were evaluated by an over-deterministic least-squares analysis of crack-opening and crack-sliding displacements respectively. The governing asymptotic expressions for crack-opening (v) and crack-sliding (u) displacement fields near the tip of a dynamically loaded stationary or steadily growing bimaterial interface crack are given by Deng [22],

$$\left\{\begin{matrix} u(r,\theta) \\ v(r,\theta) \end{matrix}\right\} = \sum_{n=0}^{\infty} r^{\frac{n+1}{2}} \frac{\mathrm{Re}[\eta_n^I (K_I)_n r^{i\varepsilon_n}]}{\sqrt{2\pi}} \left\{\begin{matrix} u_n^I(\theta) \\ v_n^I(\theta) \end{matrix}\right\} + \sum_{n=0}^{\infty} r^{\frac{n+1}{2}} \frac{\mathrm{Im}[\eta_n^{II} (K_{II})_n r^{i\varepsilon_n}]}{\sqrt{2\pi}} \left\{\begin{matrix} u_n^{II}(\theta) \\ v_n^{II}(\theta) \end{matrix}\right\} \tag{2}$$

where r and θ are the polar coordinates defined around the current crack-tip, $\varepsilon_n = \varepsilon$, $\eta_n^I = 1$, and $\eta_n^{II} = \eta$ when $n = 0, 2, 4, \ldots$, and $\varepsilon_n = 0$, $\eta_n^I = \eta$, and $\eta_n^{II} = 1$ when $n = 1, 3, 5, \ldots$, ε is the oscillation index, η is the mismatch parameter. In Eq. (2), terms

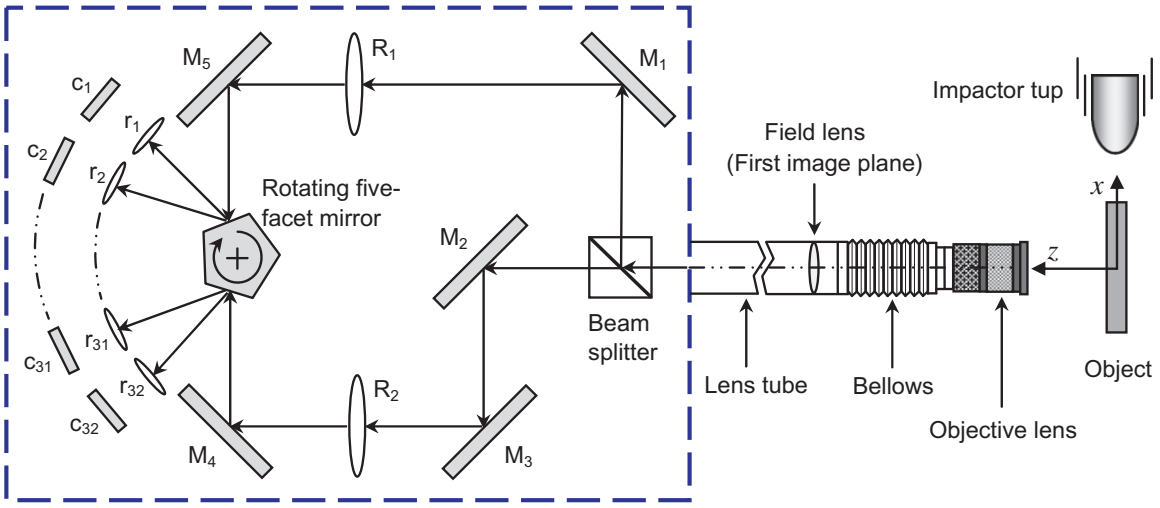

Fig. 4. Internal optical arrangement of Cordin-550 ultra high-speed digital framing camera: M_1–M_5 are mirrors; R_1 and R_2 relay lenses; r_1–r_{32} are relay lenses for CCDs; c_1–c_{32} are CCD sensors.

corresponding to $n = 0$ give the oscillatory singular crack-tip fields and the coefficients[2] of $(K_I)_n$ and $(K_{II})_n$ of the dominant terms ($n = 0$) are the dynamic SIFs respectively. In this work, SIF values were extracted using dominant terms ($n = 0$) at crack initiation and in the post-initiation regime, therefore, explicit expressions for displacement fields for steadily growing interface cracks in dissimilar isotropic materials were employed [22]:

$$u_n^I(\theta) = \frac{1}{\mu D[(n+1)^2 + 4\varepsilon^2]\cosh \pi\varepsilon} \begin{Bmatrix} (n+1)[C_1(n+2,\varepsilon,\eta) + C_1(n+2,-\varepsilon,-\eta)] \\ -2\varepsilon[S_1(n+2,\varepsilon,\eta) - S_1(n+2,-\varepsilon,-\eta)] \\ +\alpha_2(n+1)[C_2(n+2,\varepsilon,\eta) + C_2(n+2,-\varepsilon,-\eta)] \\ -2\alpha_2\varepsilon[S_2(n+2,\varepsilon,\eta) - S_2(n+2,-\varepsilon,-\eta)] \end{Bmatrix} \tag{3}$$

$$u_n^{II}(\theta) = \frac{1}{\eta\mu D[(n+1)^2 + 4\varepsilon^2]\cosh \pi\varepsilon} \begin{Bmatrix} (n+1)[S_1(n+2,\varepsilon,\eta) - S_1(n+2,-\varepsilon,-\eta)] \\ +2\varepsilon[C_1(n+2,\varepsilon,\eta) + C_1(n+2,-\varepsilon,-\eta)] \\ +\alpha_2(n+1)[S_2(n+2,\varepsilon,\eta) - S_2(n+2,-\varepsilon,-\eta)] \\ +2\alpha_2\varepsilon[C_2(n+2,\varepsilon,\eta) + C_2(n+2,-\varepsilon,-\eta)] \end{Bmatrix} \tag{4}$$

$$v_n^I(\theta) = \frac{1}{\mu D[(n+1)^2 + 4\varepsilon^2]\cosh \pi\varepsilon} \begin{Bmatrix} \alpha_1(n+1)[S_1(n+2,\varepsilon,\eta) + S_1(n+2,-\varepsilon,-\eta)] \\ -2\alpha_1\varepsilon[-C_1(n+2,\varepsilon,\eta) + C_1(n+2,-\varepsilon,-\eta)] \\ +(n+1)[S_2(n+2,\varepsilon,\eta) + S_2(n+2,-\varepsilon,-\eta)] \\ -2\varepsilon[-C_2(n+2,\varepsilon,\eta) + C_2(n+2,-\varepsilon,-\eta)] \end{Bmatrix} \tag{5}$$

$$v_n^{II}(\theta) = \frac{1}{\eta\mu D[(n+1)^2 + 4\varepsilon^2]\cosh \pi\varepsilon} \begin{Bmatrix} \alpha_1(n+1)[-C_1(n+2,\varepsilon,\eta) + C_1(n+2,-\varepsilon,-\eta)] \\ +2\alpha_1\varepsilon[S_1(n+2,\varepsilon,\eta) + S_1(n+2,-\varepsilon,-\eta)] \\ +(n+1)[-C_2(n+2,\varepsilon,\eta) + C_2(n+2,-\varepsilon,-\eta)] \\ +2\varepsilon[S_2(n+2,\varepsilon,\eta) + S_2(n+2,-\varepsilon,-\eta)] \end{Bmatrix} \tag{6}$$

where

$$\begin{aligned} C_1(n,\varepsilon,\eta) &= -r_1^{(n-1)/2} e^{\varepsilon(\pi-\theta_1)}[2\alpha_2\eta - (1+\alpha_2^2)]\cos(\tfrac{n-1}{2}\theta_1 + \varepsilon \ln r_1) \\ S_1(n,\varepsilon,\eta) &= r_1^{(n-1)/2} e^{\varepsilon(\pi-\theta_1)}[2\alpha_2\eta - (1+\alpha_2^2)]\sin(\tfrac{n-1}{2}\theta_1 + \varepsilon \ln r_1) \\ C_2(n,\varepsilon,\eta) &= -r_2^{(n-1)/2} e^{\varepsilon(\pi-\theta_2)}[2\alpha_1 - \eta(1+\alpha_2^2)]\cos(\tfrac{n-1}{2}\theta_2 + \varepsilon \ln r_2) \\ S_2(n,\varepsilon,\eta) &= r_2^{(n-1)/2} e^{\varepsilon(\pi-\theta_2)}[2\alpha_1 - \eta(1+\alpha_2^2)]\sin(\tfrac{n-1}{2}\theta_2 + \varepsilon \ln r_2) \end{aligned} \tag{7}$$

$$r_m = \sqrt{x^2 + \alpha_m^2 y^2}, \quad \theta_m = \tan^{-1}(\tfrac{\alpha_m y}{x}), \quad m = 1,2, \quad \alpha_1 = \sqrt{1 - (\tfrac{c}{C_L})^2}, \quad \alpha_2 = \sqrt{1 - (\tfrac{c}{C_S})^2}$$

$$C_L = \sqrt{\tfrac{(\kappa+1)\mu}{(\kappa-1)\rho}}, \quad C_S = \sqrt{\tfrac{\mu}{\rho}}, \quad \kappa = \tfrac{3-\upsilon}{1+\upsilon} \quad \text{for plane stress}$$

$$D = 4\alpha_1\alpha_2 - (1+\alpha_2^2)^2, \quad \varepsilon = \tfrac{1}{2\pi}\ln\tfrac{1-\beta}{1+\beta}$$

[2] Subscripts and superscripts *I* and *II* are used instead of traditional 1 and 2 notation for ease of transitioning from bimaterial fracture mechanics equations to the homogeneous material ones.

In the above equations, (x, y) are the instantaneous Cartesian coordinates aligned at the current crack-tip, c is the crack-tip velocity, C_L and C_S are longitudinal and shear wave speeds in a given material, ρ is the mass density, β is one of the Dundurs' parameter, μ and υ are shear modulus and Poisson's ratio respectively. Further, Eqs. (3)–(7) can be reduced to the form of a dynamically loaded stationary crack in the limit the crack velocity $c \to 0$. Moreover, when the oscillation index ε becomes zero then the bimaterial equations reduce to the ones for the homogeneous case.

In order to extract SIF history, the crack-opening and crack-sliding displacement fields were digitized by identifying the current crack-tip location and subsequently establishing the Cartesian and polar coordinates. A number of data points (typically 100–120) were collected in the vicinity of the current crack-tip ($0.3 < r/B < 1.5$) and [($-150° < \theta < -90°$) and ($90° < \theta < 150°$)] as it has been shown that 3D deformations are minimum in this region [23]. At each data point, v and u displacement values as well as the location of these points were stored. The digitized data were used in Eq. (2) along with an over-deterministic least-squares analysis scheme in order to estimate the two SIFs. This process was carried out for all the 32 image pairs and the SIF histories were generated. Due to mixed-mode crack growth in the inclusion vicinity, the SIFs were used to evaluate an effective SIF, K_e, and mode-mixity, ψ as,

$$K_e = \sqrt{K_I^2 + K_{II}^2} = \sqrt{K_1^2 + K_2^2} \tag{8}$$

$$\psi = \tan^{-1}\left(\frac{K_{II}}{K_I}\right) \quad \text{or} \quad \tan^{-1}\left(\frac{K_2}{K_1}\right) \quad \text{or} \quad \tan^{-1}\left(\frac{\mathrm{Im}(Ka^{i\varepsilon})}{\mathrm{Re}(Ka^{i\varepsilon})}\right) \tag{9}$$

where a is a length parameter, chosen to be unity in this study, and ε is the oscillation index as defined previously. In this work, the value of ε ranges from 0.096 to 0.156 for interface crack growth as a function of crack-tip velocity at the inclusion–matrix interface and 0 elsewhere for homogeneous crack propagation.

4. Experimental results

4.1. Crack path and surface deformation histories

Edge cracked epoxy specimens embedded with weakly and strongly bonded symmetric ($e = 0$) and eccentric ($e = 3d/4$) cylindrical glass inclusions were subjected to globally symmetric impact loading. Photographs of four fractured samples from each configuration representing different crack-inclusion interaction scenarios are shown in Fig. 5. The impact point is located on the top edge of each image and the initial crack-tip is at the bottom edge as indicated. The location of cylindrical glass inclusion is shown by a dotted circle and the vertical broken arrow indicates the direction of crack propagation. In each configuration, it is evident that after initiation the crack propagates self-similarly until it reaches the inclusion–matrix interface vicinity and significant differences in crack paths occur subsequently. For the case of a symmetrically located weakly bonded inclusion ($e = 0$), once inclusion–matrix debonding occurs the crack is momentarily arrested after it circumscribes the interface covering a distance of approximately half the inclusion circumference and then reinitiates in a mode-I fashion with approximately zero offset distance with respect to the initial crack path. On the other hand, in the case of symmetrically located strongly bonded inclusion ($e = 0$), when the crack reaches the inclusion vicinity, it is initially arrested. Further it circumvents the inclusion to a lesser extent when compared to the weakly bonded counterpart and then deflected away from inclusion–matrix interface before propagating in a nearly mode-I fashion at an offset (of about half the inclusion diameter). When the inclusion is not in the prospective crack path and positioned eccentrically ($e = 3d/4$), the crack trajectories in the inclusion vicinity are different compared to the symmetrically located inclusion case. In the case of weakly bonded inclusion with $e = 3d/4$, it is clearly evident that crack is attracted towards the weak inclusion–matrix interface and leaves inclusion vicinity and tends to achieve initial crack path, whereas when the inclusion is strongly bonded to the matrix, it is interesting to note that as the crack approaches the inclusion vicinity the stronger inclusion–matrix interface forces the crack to deflect away from the inclusion followed by crack propagation in a mode-I path. (In all the photographs of fractured specimens in Fig. 5, it can be seen that just before the upper edge of the specimens, the crack growth is affected by a combination of free-edge and impact point interactions.)

From each experiment, a selected speckle image of $30 \times 30\ \mathrm{mm}^2$ region of interest is shown in Fig. 6 (images rotated clockwise by 90° relative to Fig. 5). The time instant (t) at which the images were recorded after impact is shown on each image and the current crack-tip is indicated by an arrow. From Fig. 5 and deformed speckle images in Fig. 6, it is worth noting the effects of inclusion location and inclusion–matrix adhesion strength on crack trajectories. For symmetrically located inclusion ($e = 0$) the crack front is trapped by the weaker interface compared to the stronger one. In the eccentric inclusion cases, the crack is clearly attracted by the weak inclusion–matrix interface whereas the strong inclusion–matrix interface leads to crack deflection mechanism.

Two representative speckle images along with the corresponding full-field crack-opening (v-field or displacement along the y-axis) and crack-sliding (u-field or displacement along the x-axis) displacement contours for weakly and strongly bonded inclusion specimens at eccentricity $e = 0$ are shown in Fig. 7. In this work, displacements were obtained as a matrix of 40×40 data points in the inclusion–matrix vicinity for each image pair and full-field displacement contours with 2 μm intervals corresponding to the resolution of the method [19] were generated. In the v-field, contour lines (magnitude) are symmetric relative to the crack path before the crack interacts with the inclusion suggesting mode-I conditions. The discon-

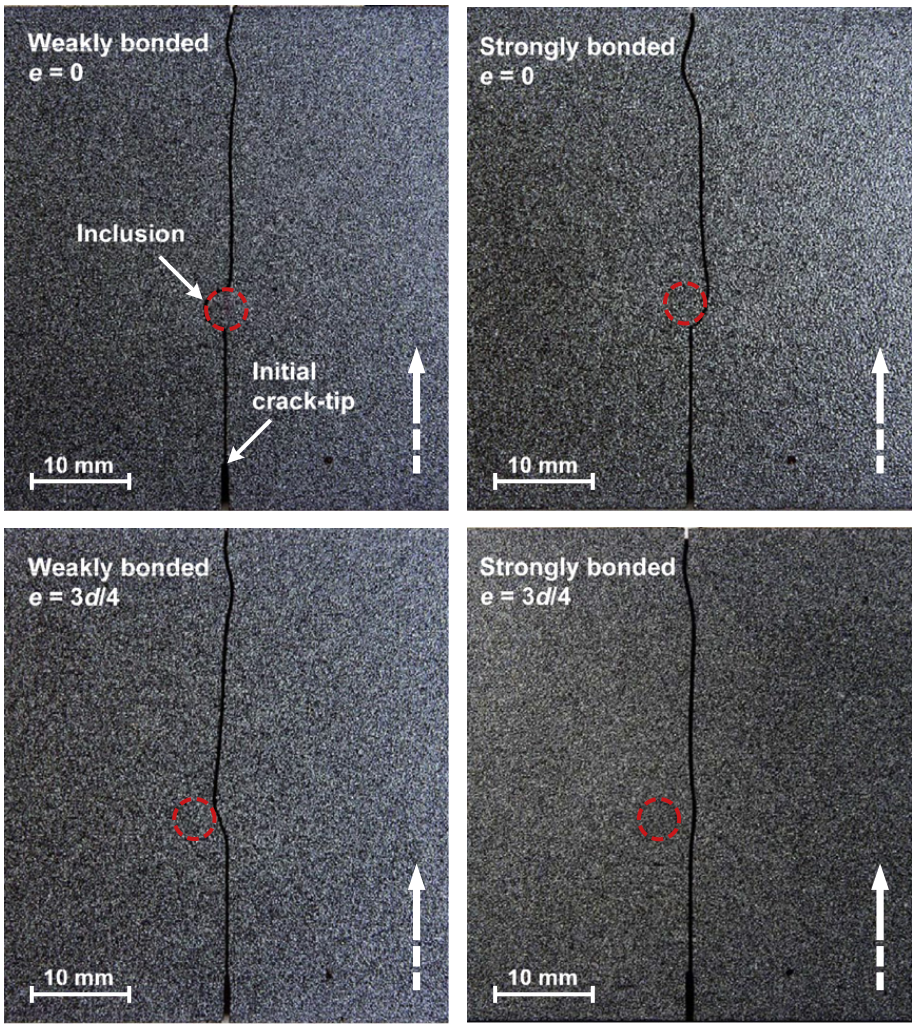

Fig. 5. Photographs of fractured glass inclusion specimens showing different crack–inclusion interaction scenarios. The black dot adjacent to initial crack-tip denotes the reference mark and the broken arrow indicates crack propagation direction.

tinuity in displacements around the inclusion can be seen when the crack reaches the inclusion. Also, in case of the weakly bonded inclusion, contour lines around the inclusion become discontinuous when compared to the ones for strongly bonded since debonding of the inclusion occurs in the former. Further, after the crack propagates beyond the inclusion, displacement contours are rather symmetric in the weakly bonded case. This is absent in the strongly bonded counterpart and contour lines are asymmetric as a result of crack deflection followed by crack growth at an offset with respect to the initial crack path. In the u-field, the contour lines show a set of isolines emerging from right-hand side of the contour plots due to impact occurring on the edge of the specimen facing the initial crack-tip. Also, it should be noted that the contours lines within the inclusion are nearly parallel to each other and equally spaced implying rigid rotation of the inclusion with the matrix after debonding.[3]

4.2. Experimental repeatability

Multiple experiments were conducted for both inclusion eccentricities as well as adhesion strengths to ensure repeatability in fracture behavior as well as measurements. Fig. 8a and b shows right-half ligaments of three fractured glass inclusion specimens for each weakly bonded inclusion with $e = 0$ and strongly bonded inclusion with $e = 3d/4$ configurations respectively. A high degree of reproducibility in crack paths including macroscale surface features is clearly evident. More importantly, distinctly different crack–inclusion interaction scenarios can be seen in these two configurations. As noted earlier from Fig. 5, all fractured specimens shown in Fig. 8 depict similar crack trajectories including crack attraction and deflection mechanisms. The ligaments holding glass inclusions in Fig. 8a shows a good repeatability in the crack path around inclusion–

[3] It should be noted here that despite the camera being a state-of-the-art instrument, the spatial resolution is still far from being optimum for this study. This limits our ability to capture deformation details accurately near the interface without magnifying the image. If magnified, however, the information regarding global deformations will be greatly compromised and hence not used in this work.

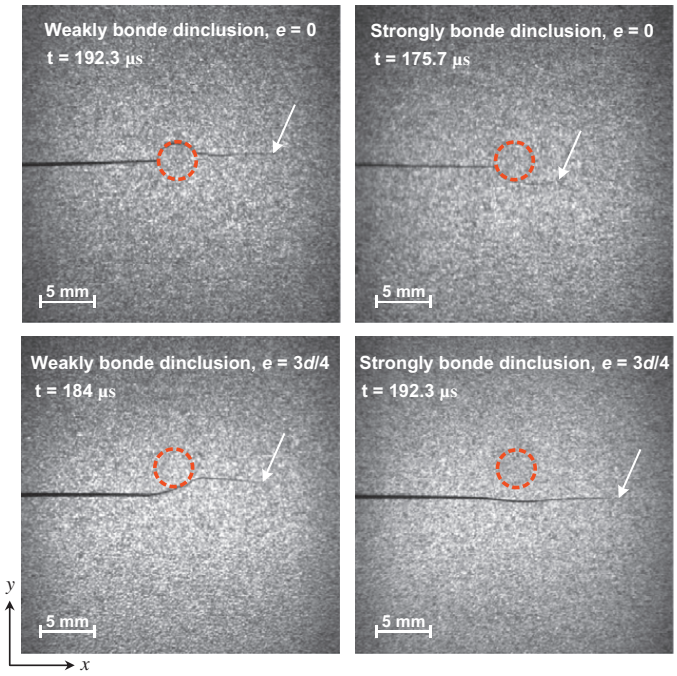

Fig. 6. Selected speckle images of 30 × 30 mm^2 region of interest recorded at a framing rate of 300,000 frames per second. The broken circle represents inclusion location and arrow indicates current crack-tip position.

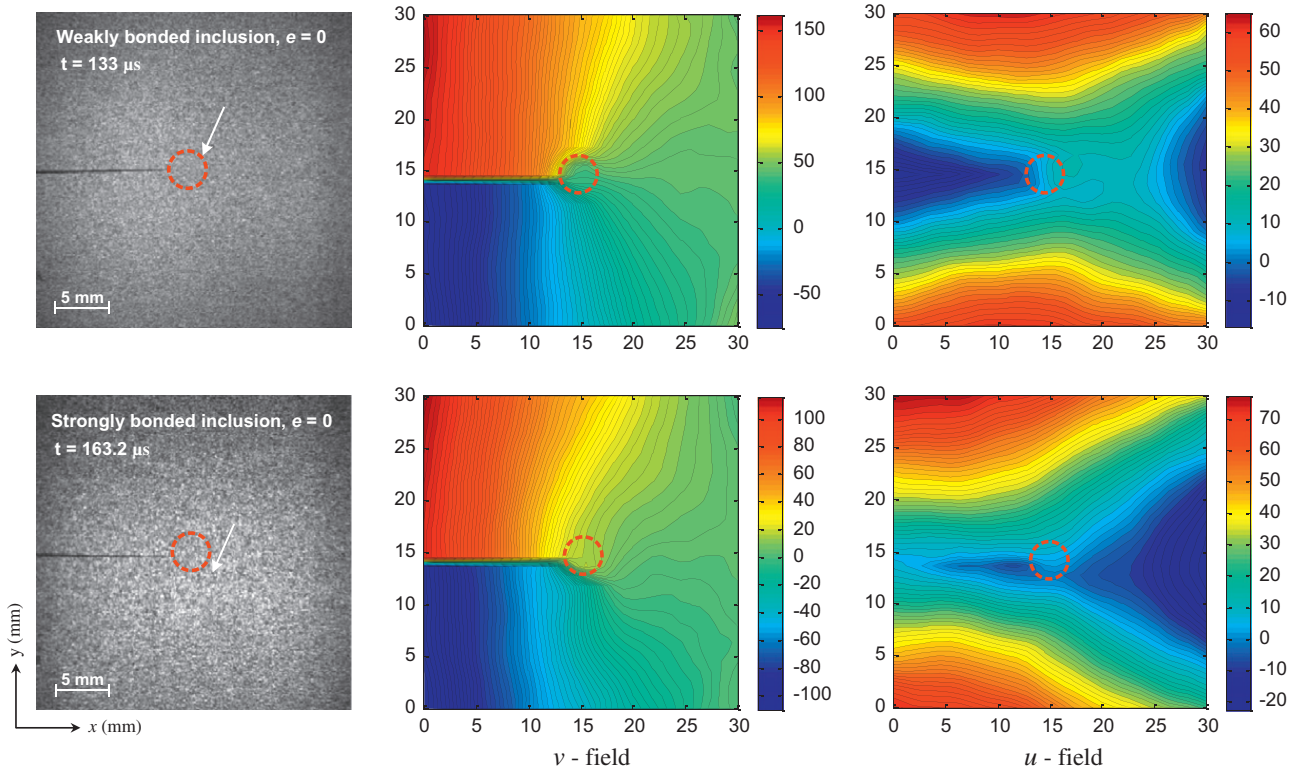

Fig. 7. Acquired speckle images of 30 × 30 mm^2 region of interest for weakly and strongly bonded inclusion specimens at eccentricity, $e = 0$ with full-field crack-opening (v-field) and crack-sliding (u-field) displacement contours. Contour interval is 2 μm. Color-bars indicate displacement in micrometers. The location of cylindrical glass inclusion is represented by broken circle and arrow indicates the current crack-tip position in the photographed images. (For interpretation of the references to color in this figure legend, the reader is referred to the web version of this article.)

matrix whereas crack deflection is clearly visible in each ligament shown in Fig. 8b. Also, the photographs in Fig. 8 demonstrate that the crack propagated in dominant mode-I fashion *before* and *after* the encounter with the inclusion.

Fig. 9a and b depicts crack growth histories and SIF histories respectively for three identical glass inclusion specimens for weakly bonded symmetric configuration, ($e = 0$) demonstrating repeatability of force history measurements. Here t_i indicates

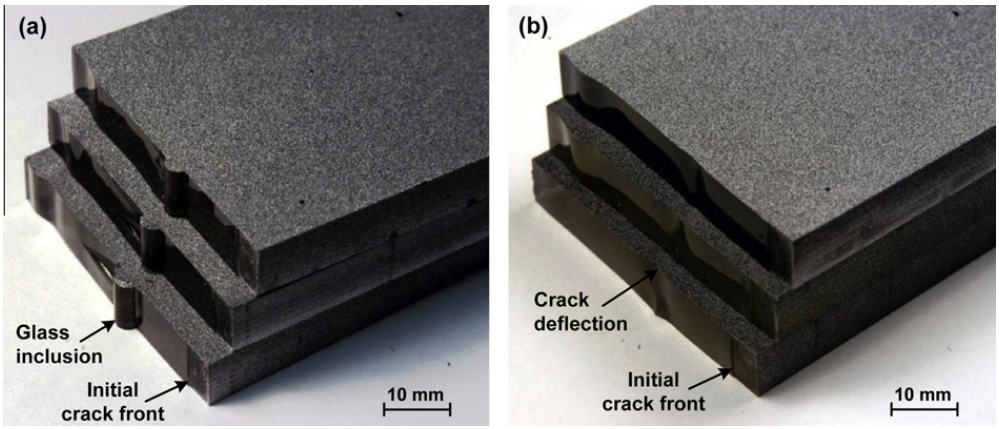

Fig. 8. Right-half ligaments of fractured glass inclusion specimens demonstrating experimental repeatability for (a) weakly bonded inclusion with $e = 0$ (b) strongly bonded inclusion with $e = 3d/4$.

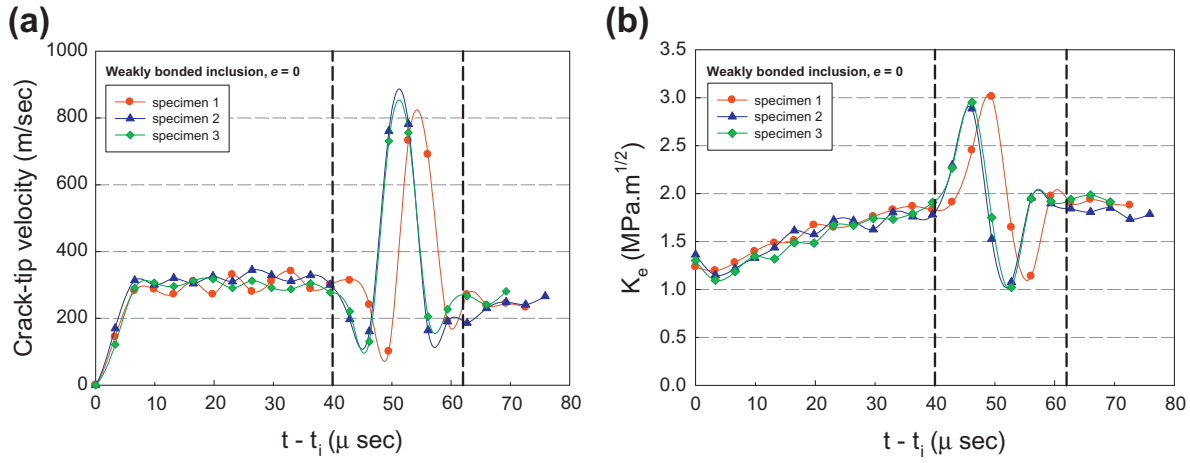

Fig. 9. (a) Crack velocity histories, and (b) effective stress intensity factor histories, for three identical weakly bonded inclusion specimens with eccentricity $e = 0$ demonstrating repeatability of experimental measurements. The region between vertical broken lines represents crack–inclusion vicinity.

the time at crack initiation after impact. The region between the two vertical broken lines suggest the duration of crack–inclusion interaction qualitatively. In Fig. 9a following initiation, crack accelerated and attained a steady state velocity of approximately 320 m/s. A drop in velocity as the crack encounters the stiff inclusion is evident before climbing to a relatively high value of ~780 m/s and dropping back to 200 m/s after it departs the inclusion vicinity. All the three specimens show excellent repeatability in crack velocity profiles *before* and *after* the crack-tip encounters the inclusion (and only a small deviation can be noticed for one of the specimens due to debond path selection around the inclusion due to local inhomogeneities). The effective SIF (K_e) histories obtained using the method detailed earlier for the same three specimens are shown in Fig. 9b. The K_e profiles show excellent repeatability (from the perspective of dynamic fracture experiments) throughout the fracture event, and similar to crack velocity histories, only minor deviations in SIF can be seen in the crack–inclusion vicinity. In each specimen, the effective SIF, at initiation is ~1.3 MPa $m^{1/2}$. Following crack initiation, a noticeable drop in K_e can be seen due to unloading near the initial notch tip. Subsequently, K_e continues to increase until a value of ~1.8 MPa $m^{1/2}$ is attained and a steady state K_e prevails until the crack encounters the inclusion. In the crack–inclusion vicinity, K_e attains a maximum value of ~3.0 MPa $m^{1/2}$ and drops back to a value of ~1.0 MPa $m^{1/2}$ followed by a steady state K_e value of ~1.9 MPa $m^{1/2}$ after the crack leaves the inclusion vicinity. Therefore, the K_e values are relatively higher when the crack-tip is very close to or lodged into the interface and decreases momentarily as the crack departs the inclusion vicinity.

The tup and anvil load histories were recorded for each experiment and are shown in Fig. 10 for the three identical symmetrically located weakly bonded inclusion specimens. In this plot, again an excellent repeatability in tup load as well as in left and right support reaction histories is quite evident for all three specimens. The occurrence of more than one peak indicates multiple contacts between the specimen and the impactor. In these experiments, the crack was initiated at about 120 μs and complete fracture of the specimen occurred in approximately 220 μs after impact. Thus, the initial peak of the tup load history is relevant in these experiments. The reaction histories were captured by left and right instrumented support anvils and it can be seen that supports feel the reaction force only after 300 μs by which time the crack had already traversed the specimen width. This shows that reaction forces from support anvils do not contribute to the crack initiation

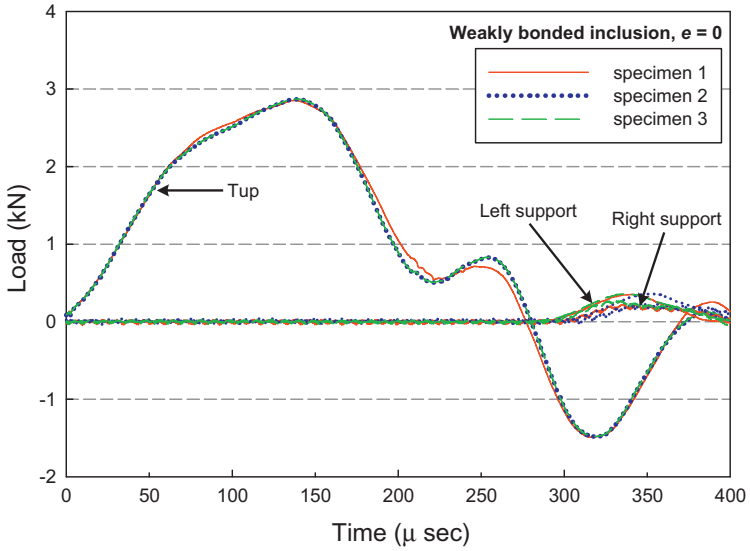

Fig. 10. Experimental repeatability in load histories for three identical weakly bonded inclusion specimens with eccentricity, $e = 0$.

and crack growth in the specimens, suggesting that a free-free cracked beam should suffice analytical or computational modeling of these experiments.

Thus, the similarity of crack-tip velocity profiles, SIFs histories, tup load and support reaction histories in multiple samples indicates the robustness and repeatability of the experiments performed and the optical method employed in this work. Similar repeatability tests have also been carried out successfully for other configurations and have been avoided here for brevity.

4.3. Crack growth histories

The crack length histories for each specimen configuration are plotted in Fig. 11. In this plot, the crack-initiation time is denoted by $t - t_i = 0$ so that the positive and negative values correspond to the post-initiation and pre-initiation periods respectively. Fig. 11a shows crack length histories for weakly and strongly bonded symmetric inclusion. Following initiation, a monotonic crack growth is evident and as crack approaches the inclusion, the amount of crack extension drops modestly before increasing at a much faster rate in the crack–inclusion vicinity as it gets attracted and completely arrested by the weak inclusion–matrix interface. Unlike the weakly bonded inclusion case, the crack growth is slower in the region *before* the crack interacts with the strongly bonded inclusion and in the inclusion vicinity a sudden jump in crack length can be noticed but this jump is lower than the one for the weakly bonded case. As it leaves the inclusion vicinity, the crack grows nearly at the same rate in both weakly and strongly bonded inclusion cases. The crack length histories when the inclusion is located eccentrically are shown in Fig. 11b. In these, before the crack reaches the inclusion vicinity it grows at a constant rate and the crack extension histories for both weakly and strongly bonded inclusion cases coincide. In the crack–inclusion vicin-

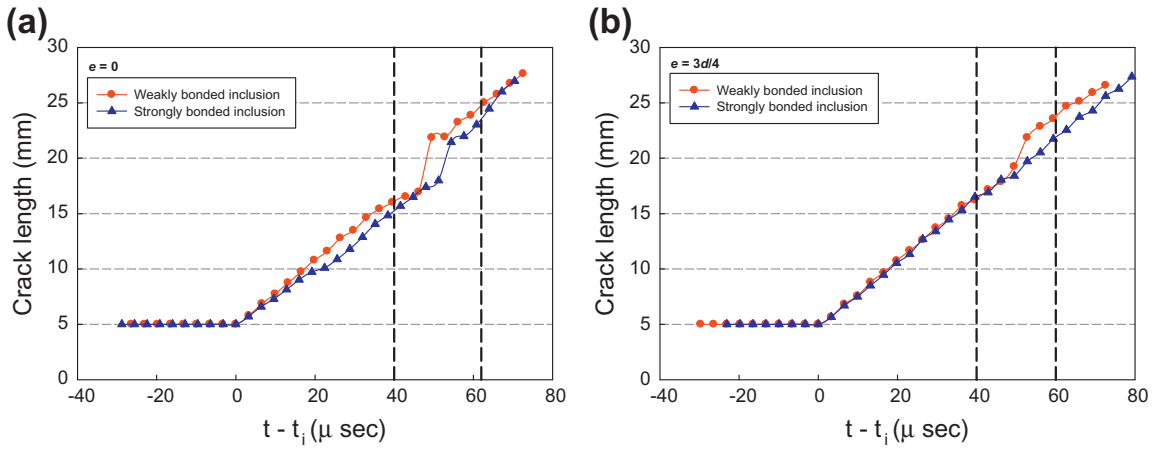

Fig. 11. Crack length histories for weakly and strongly bonded inclusion specimens with eccentricity (a) $e = 0$, (b) $e = 3d/4$. The region between vertical broken lines represents crack–inclusion vicinity.

ity and after that, the weakly bonded inclusion shows a faster crack growth compared to the strongly bonded case in which crack growth remains nominally undisturbed.

The instantaneous values of crack extension were measured by locating the crack-tip in the digitized images. These were subsequently used to estimate crack velocity histories and are plotted in Fig. 12a and b respectively with eccentricities, $e = 0$ and $3d/4$ for weakly and strongly bonded inclusions. The effect of the adhesion strength on crack velocity can be seen in these plots for both inclusion eccentricities. In Fig. 12a, the symmetrically located inclusion case shows nearly similar velocity profiles until the crack encounters the inclusion. A drop in velocity can be seen in weakly bonded inclusion case when the crack is slowed at inclusion–matrix interface just before re-initiation. The crack velocity drops to ~100 m/s and 210 m/s for weakly and strongly bonded inclusions respectively. The re-initiation velocities in weakly and strongly bonded inclusions reach ~780 m/s and ~600 m/s respectively. Fig. 12b shows velocity data for weakly and strongly bonded inclusions when the inclusion is located eccentrically. Again, the velocity profiles are nearly similar until the crack reaches in the inclusion vicinity. For the weakly bonded case the maximum velocity reaches ~600 m/s as the crack is initially arrested at the inclusion by the weak interface, whereas a constant decrease in velocity can be seen for strongly bonded case as the crack circumvents in the inclusion vicinity.

4.4. Stress intensity factor histories

The effect of inclusion–matrix adhesion strength on SIFs is represented by Fig. 13a and b for $e = 0$ and $3d/4$ cases, respectively. Fig. 13a shows effective SIF histories for weakly and strongly bonded cases when the inclusion is located symmetrically. For both specimens, the effective SIF, K_e at initiation is ~1.3 MPa $m^{1/2}$. After initiation, a slight drop in K_e is evident, and K_e continues to increase until it reaches a steady state value of ~1.8 MPa $m^{1/2}$. The K_e is slightly higher for weakly bonded case compared to strongly bonded one *before* the crack reaches the inclusion proximity. In the crack–inclusion vicinity, for the weakly bonded case, K_e attains a maximum value of ~2.9 MPa $m^{1/2}$ before dropping to ~1.0 MPa $m^{1/2}$ whereas for the strongly bonded counterpart the maximum value of K_e is ~2.1 MPa $m^{1/2}$ before dropping to ~0.9 MPa $m^{1/2}$ followed by a steady state K_e value of ~1.7 MPa $m^{1/2}$ in both specimens after the crack leaves the inclusion vicinity. A steep drop in K_e is quite evident for both weakly bonded inclusions when the crack is in the close proximity of the inclusion. This rise and fall in K_e values in the crack–inclusion vicinity is expected due to interfacial crack growth behavior around the stiff-compliant inclusion–matrix interface.

Fig. 13b shows effective SIF histories for weakly and strongly bonded eccentrically located inclusions. Similar to the symmetric cases, K_e at initiation is ~1.3 MPa $m^{1/2}$ followed by a slight drop and a monotonic increase until it attains a steady state value of ~1.9 MPa $m^{1/2}$ for both specimens. In the inclusion proximity, for the weakly bonded inclusion case, K_e increases up to ~2.4 MPa $m^{1/2}$ and subsequently drops to ~1.1 MPa $m^{1/2}$ whereas for strongly bonded one this remains unperturbed and then K_e values are nearly equal and overlap over each other as the crack propagates away from the inclusion proximity.

4.5. Mode-mixity histories

The mode-mixity (ψ) is plotted against time in Fig. 14 for weakly and strongly bonded inclusion specimens with an eccentricity of $e = 0$ and $3d/4$. The mode-mixity histories for both bond strengths for symmetric case are plotted in Fig. 14a. Following initiation, an oscillatory behavior of mode-mixity for about 20 μs can be seen. These oscillations can be attributed to experimental errors and/or stress waves due to crack initiation. Beyond these initial perturbations, a constant and positive ψ

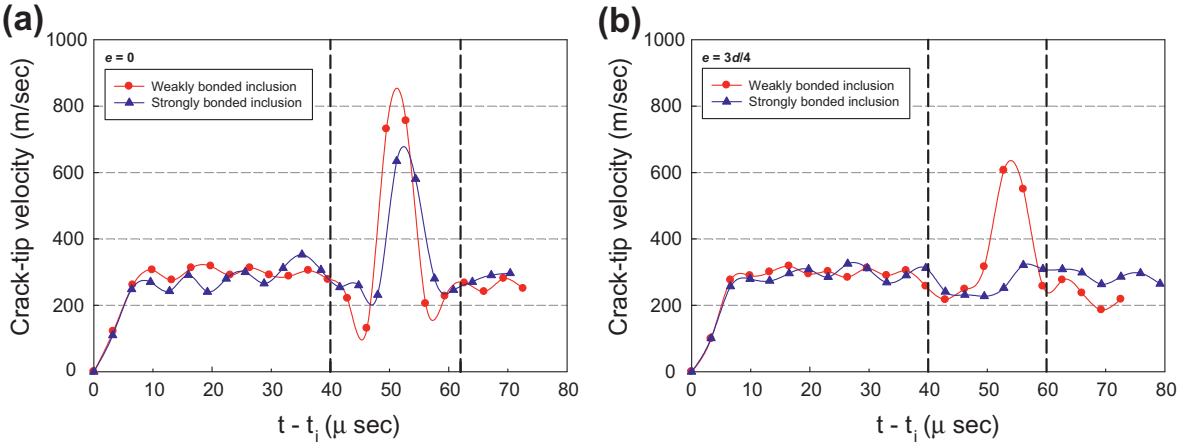

Fig. 12. Crack-tip velocity histories for weakly and strongly bonded inclusion specimens with eccentricity: (a) $e = 0$, (b) $e = 3d/4$. The region between vertical broken lines represents crack–inclusion vicinity.

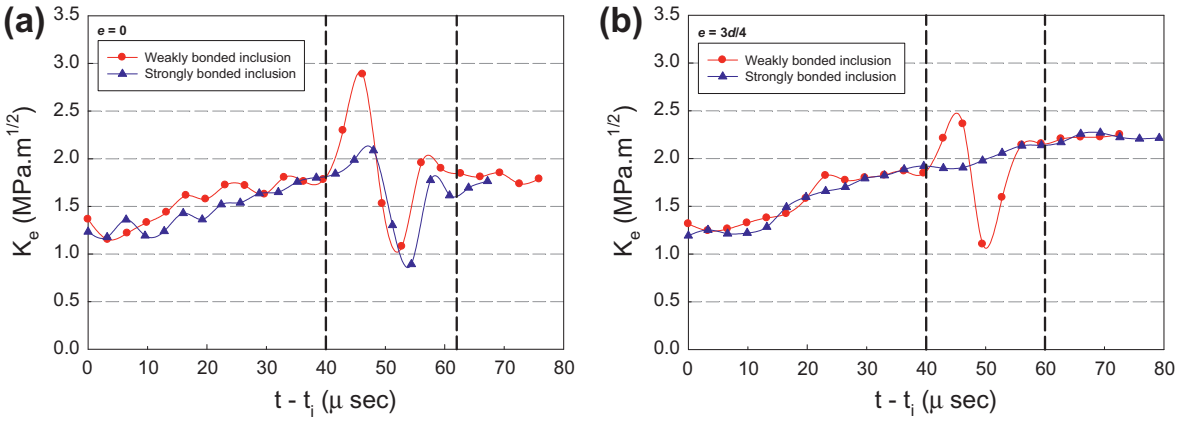

Fig. 13. Effective stress intensity factor histories for weakly and strongly bonded inclusion specimens with eccentricity: (a) $e = 0$, (b) $e = 3d/4$. The region between vertical broken lines represents crack–inclusion vicinity.

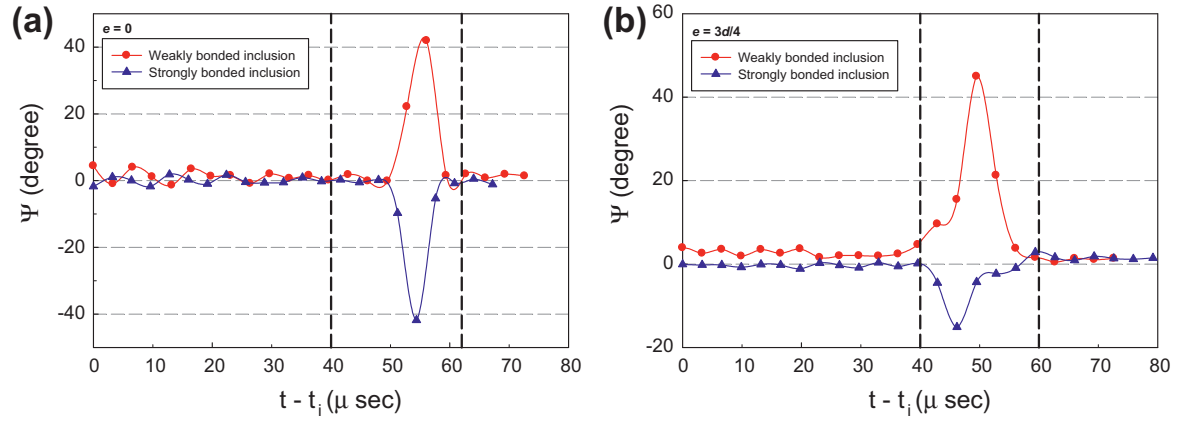

Fig. 14. Mode-mixity histories for weakly and strongly bonded inclusion specimens with eccentricity: (a) $e = 0$, (b) $e = 3d/4$. The region between vertical broken lines represents crack–inclusion vicinity.

of about 2° is seen before the crack interacts with the inclusion. (Within the data extraction errors this value can be practically assumed to be zero for an observed self similar growth.) When the crack-tip is in the inclusion vicinity a positive mode-mixity of approximately +42° is seen for the weakly bonded inclusion specimen whereas a negative mode-mixity of about −41° is observed for strongly bonded case. In both cases, after the crack leaves inclusion proximity, ψ attains a constant value of nearly 2°.

In Fig. 14b for the asymmetric inclusion configuration, after the initial oscillatory period, the weakly bonded inclusion shows a monotonic increase in ψ as the crack approaches the inclusion vicinity whereas ψ remains close to zero in the strongly bonded case. Different mode-mixity behaviors can be seen as the crack nears the inclusion for both weakly and strongly bonded inclusion cases. In the case of weakly bonded inclusion specimen, positive mode-mixity values are seen with a maximum of +45°, indicating a significant attraction of the crack-tip by the weak interface. Contrary to the weakly bonded case, the negative mode-mixity behavior is noticed with a value of −15° suggesting that the crack is being repelled by the strong interface. The opposite mode-mixity behaviors are consistent with the crack trajectories shown in Fig. 5 for all inclusion configurations and bond strengths indicating that the crack is being attracted towards the weakly bonded inclusion, whereas it is deflected away from the strongly bonded inclusion. Once the crack leaves the inclusion vicinity, mode-mixities tend to approach zero and crack propagation occurs under dominant mode-I conditions in both weakly and strongly bonded inclusion specimens.

The crack growth results show similar crack trajectories and crack-tip velocity profiles as reported in Ref. [12] but with a higher temporal resolution. Even though the previous work has used modestly different specimen geometry, the SIF and mode-mixity histories reported here are qualitatively similar with much greater detail particularly in the inclusion vicinity and during crack growth past the inclusion. Quantitative differences, on the other hand, are primarily due to refined data analysis before, during, and after interaction with the inclusion in this current work, made possible by better temporal resolution, choice of the field quantity and adoption of appropriate analysis based on whether the crack-tip is in the matrix or at the matrix-inclusion interface. Unlike the previous work, the effective SIFs extracted from the measured full-field displacements in the current study show details such as presence of a spike in values corresponding to high crack velocities in the

inclusion vicinity. For example, in the inclusion proximity for the case of weakly bonded inclusion ($e = 0$), K_e attains a maximum value of ~3.0 MPa $m^{1/2}$ before dropping to ~1.0 MPa $m^{1/2}$ as the weak inclusion-matrix interface crack propagates and reinitiates. Such details could not be achieved in the previous work using CGS once the crack reached the inclusion vicinity.

4.6. Fracture surface roughness

It is well recognized [24,25] that post-mortem analysis of fracture surfaces often reveal underlying failure mechanisms and the associated energy dissipation characteristics. Accordingly, to further understand the differences in crack growth behaviors as a result of inclusion location and inclusion–matrix adhesion strength, the fracture surfaces were studied. Both qualitative and quantitative examination of fractured surfaces was performed using optical microscopy and surface profilometery. Quantitative micro-measurements were carried out using a Dektak-150 stylus profiler with a stylus of root radius of 12.5 μm. The fracture surface profiles were scanned at two different zones, just *before* and just *after* crack–inclusion interaction. Fig. 15 represents a schematic of crack growth in a glass inclusion specimen and the regions of interest (x–z plane) for roughness measurements are being highlighted *before* and just *after* crack–inclusion interaction. Here x – represents scanning length along which stylus was moved and y – denotes the asperity height. The scanning length of $x = 2$ and 5 mm was chosen in the region *before* and *after* crack–inclusion interaction respectively. The data was recorded at 3–4 different scan lines at different z – locations on either side of the centerline within the regions of interest. The digitized data obtained from the surface profiler was processed to get average roughness *Ra* using,

$$Ra = \frac{1}{N}\sum_{n=1}^{N}|y(x)| = \frac{1}{L}\int_0^L y\,dx \tag{10}$$

where, N is the total number data points collected, L is the scan length and (x, y) are defined as shown in Fig. 15.

Fig. 16 shows a few representative surface profiles for weakly and strongly bonded inclusion specimens for both eccentricities. (The region between vertical broken lines represents the location of the inclusion where scanning was not performed.) The profiles between 0–2 mm and 6–11 mm represent the fracture surfaces just *before* and *after* crack–inclusion interaction. From Fig. 16 it can be seen that each surface profile is qualitatively different from each other. The effects of inclusion–matrix bond strength as well as inclusion location are quite evident from these profiles. In Fig. 16a, for symmetrically located inclusion ($e = 0$) surface profile amplitudes are much smaller in the region *before* crack interacts with inclusion when compared to the surface profiles *after* crack–inclusion interaction. In the region where the crack leaves the inclusion vicinity surface profiles are different from each other with larger amplitude and higher frequency content for the weakly bonded case when compared to the strongly bonded one. Further, the wavelength is smaller in the former compared to the latter. The surface profiles for $e = 3d/4$ case are shown in Fig. 16b where similar features can also be noticed. When comparing the sur-

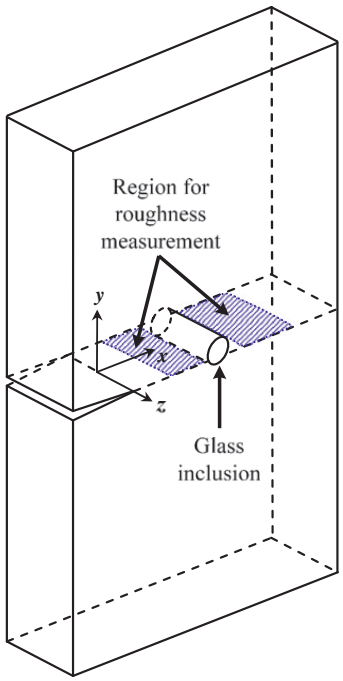

Fig. 15. Schematic representing crack growth in a glass inclusion specimen and the region selected for roughness measurement (x–z plane) *before* and *after* crack–inclusion interaction is also shown.

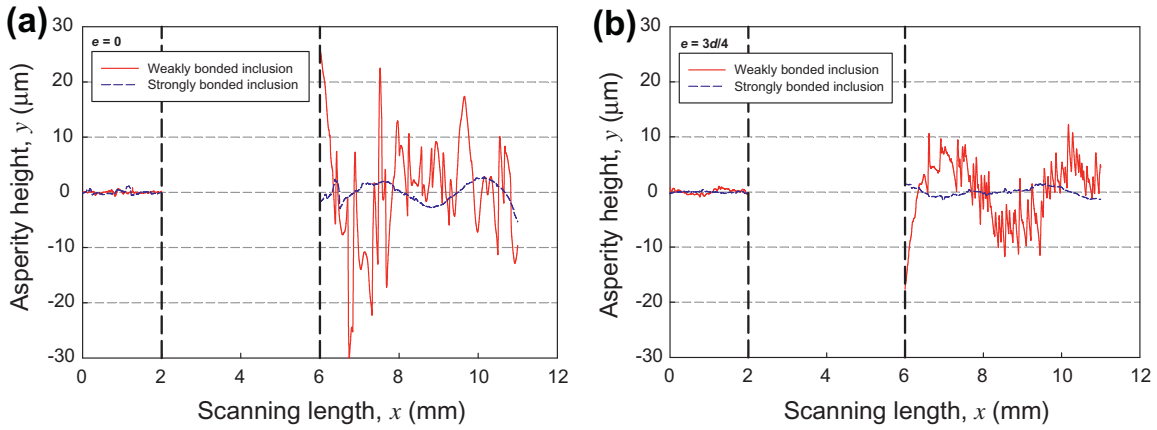

Fig. 16. Representative fracture surface profiles for weakly and strongly bonded inclusion specimens for eccentricity: (a) $e = 0$, (b) $e = 3d/4$. The region between vertical broken lines represents inclusion location.

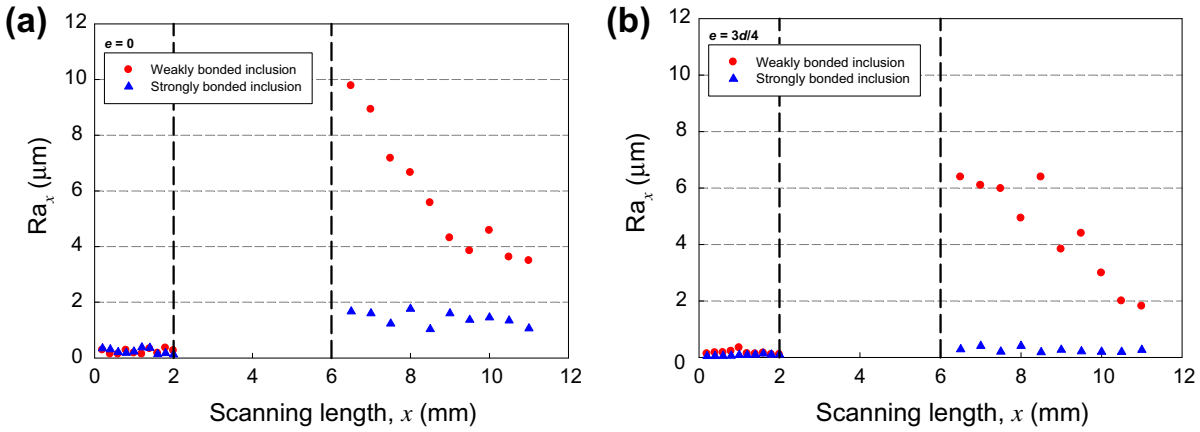

Fig. 17. Variation of fracture surface roughness along scanning length for weakly and strongly bonded inclusion specimens with eccentricity: (a) $e = 0$, (b) $e = 3d/4$. The region between vertical broken lines represents inclusion location.

face profiles in the region *after* crack–inclusion interaction for both $e = 0$ and $3d/4$ cases, the surface profiles in asymmetric case show relatively smaller amplitudes with high frequency content when compared to the symmetric case.

In order to quantify the variation of Ra along the direction of crack propagation, a longitudinal average roughness parameter Ra_x is used. The Ra_x was obtained by calculating Ra from data points collected for every 0.2 mm scan length in the region *before* and 0.5 mm scan length in the region *after* crack–inclusion interface. The Ra_x values thus obtained are plotted against scanning length in Fig. 17. The variation of Ra_x along scan length for symmetrically located inclusion ($e = 0$) is shown in Fig. 17a. The Ra_x values are nearly equal in the region *before* the crack interacts with the inclusion for both bond strengths. On the other hand in the region *after* crack–inclusion interaction Ra_x values are much higher and show a decreasing trend for the weakly bonded inclusion when compared to the strongly bonded one where Ra_x values are almost constant. Similar trends can be seen for the case of $e = 3d/4$ and are shown in Fig. 17b. In this case Ra_x values are relatively smaller than the $e = 0$ case.

From the differences observed in these surface profiles and average roughness parameters shown in Figs. 16 and 17, it can be concluded that the weakly bonded glass inclusion results in much higher fracture surface roughness when compared to the strongly bonded counterparts during dynamic crack growth. The average roughness values are nearly equal in the region *before* the crack interacts with the inclusion but the same are higher in the region *after* the crack leaves the inclusion proximity. Considering the effect of the inclusion location on roughness, the specimens with $e = 0$ configuration show relatively higher roughness values compared to $e = 3d/4$. In Figs. 16 and 17, the surface roughness can be viewed as the combination of the high frequency content indicating local energy dissipation and the low frequency content suggesting the tortuosity in crack path. The tortuosity is present in all cases; however there is always a limit on the amplitude of tortuosity. Therefore, the high frequency content comes into the picture when there is a need of further energy dissipation, that is, in the weakly bonded case. Furthermore, the amplitude of high frequency content depends upon the magnitude of the energy dissipation.

The differences in toughening mechanism can also be explained by microscopically examining the fracture surfaces. Fig. 18 shows optical micrographs of fracture surfaces (x–z plane, see Fig. 15) for $e = 0$ case for both bond strengths. These

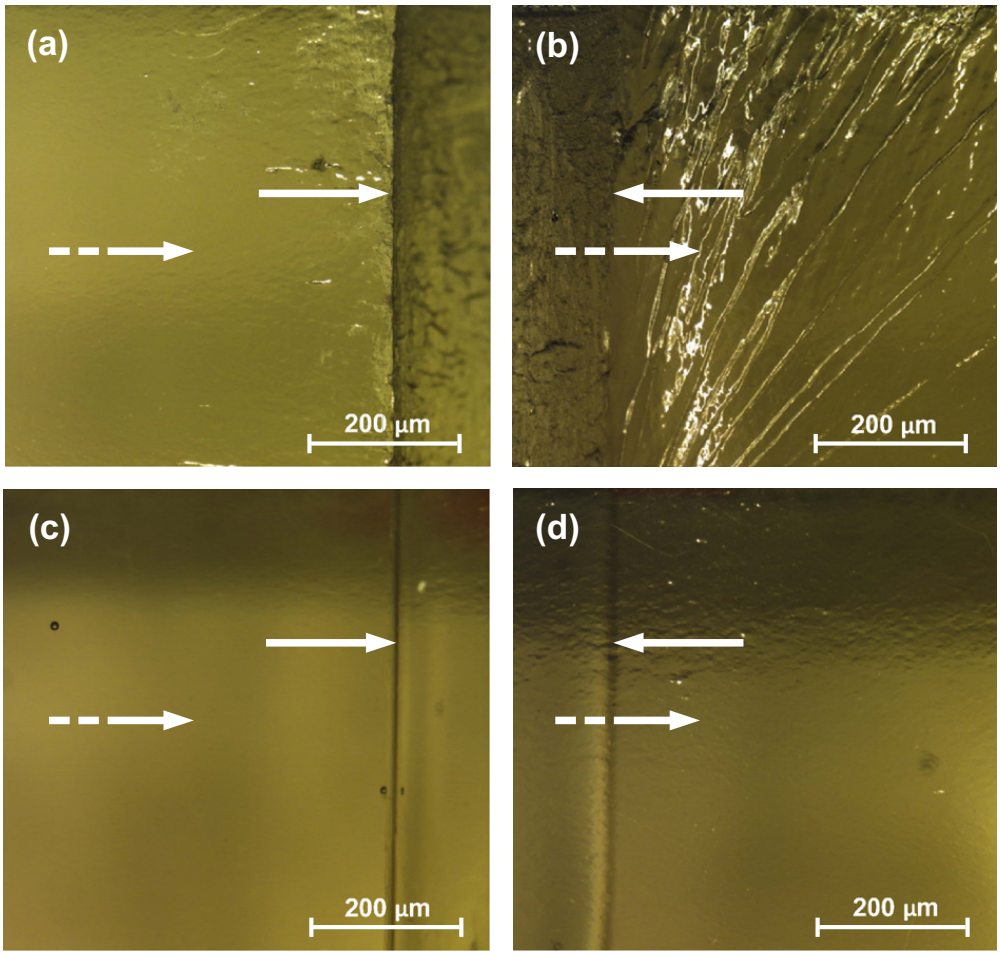

Fig. 18. Optical micrographs of fractured surfaces (x–z plane) of glass inclusion specimens for $e = 0$: (a) Region *before* crack interacts with *weakly* bonded inclusion. (b) Region *after* crack interacts with *weakly* bonded inclusion. (c) Region *before* crack interacts with *strongly* bonded inclusion. (d) Region *after* crack interacts with *strongly* bonded inclusion. The broken arrow indicates the direction of crack propagation and solid arrow shows inclusion–matrix interface.

micrographs show regions *before* and *after* crack–inclusion interaction. Here, the inclusion–matrix interface can also be seen and being indicated by a solid arrow. The broken arrow indicates the direction of crack propagation. Fig. 18a and b depicts fractured surface of the weakly bonded glass inclusion specimen *before* and *after* crack–inclusion interaction. In the region just *before* the crack reaches the inclusion, the fracture surface is relatively smooth when compared to the region *after* crack–inclusion interaction resulting in micro-cracks and river-bed patterns at an angle to the direction of crack propagation. On the other hand, in Fig. 18c and d the fracture surfaces are essentially smooth *before* as well as *after* crack–inclusion interaction. The case of weakly bonded inclusion reveals a highly transient fracture *after* the crack reinitiates at the crack–inclusion interface, showing a highly textured surfaces containing a large number of river markings, and micro-cracks. The presence of higher surface ruggedness in this case suggests greater energy dissipation consistent with the higher roughness measurements reported in Fig. 17.

5. Conclusions

In this work, crack–inclusion interactions under dynamic stress-wave loading conditions were investigated optically using digital image correlation method used in conjunction with high-speed photography. Edge cracked epoxy specimens embedded with two types of cylindrical glass inclusions, weakly and strongly bonded and located at two different eccentricities, $e = 0$ and $3d/4$ with respect to the initial crack path were studied. The interactions between a dynamically propagating mode-I crack and an isolated stiff inclusion were recorded and analyzed. Fractured specimens show different crack trajectories and crack velocities for each inclusion location and inclusion–matrix bond strengths. For specimens with symmetric inclusion ($e = 0$) higher crack velocities were observed when compared to the asymmetric inclusion ($e = 3d/4$) cases. The crack velocities also varied with the inclusion–matrix adhesion strength. Higher crack speeds were observed for weakly bonded inclusion cases compared to the strongly bonded counterparts. The dynamically propagating crack is attracted

and arrested by the weakly bonded inclusion interface whereas it is being deflected away by the stronger one. The inclusion location and inclusion–matrix interfacial strength also affect the fracture parameters such as stress intensity factor (SIF) and mode-mixity. In the weakly bonded symmetric inclusion case, the effective SIF (K_e) increases monotonically, attains a steady state value and jumps by nearly 65% above the steady state value before dropping to the steady state value. In the weakly bonded eccentric inclusion case, the K_e variation is relatively smaller near to the inclusion vicinity when compared to the symmetric case. On the other hand, in the case of strongly bonded inclusion, the K_e values are relatively lower in the inclusion proximity when compared to the weakly bonded cases. The mode-mixity are of opposite signs suggesting crack attraction and deflection mechanisms for weak and strong inclusion–matrix adhesion strengths, respectively. Quantitative and qualitative examination of fracture surfaces in the regions *before* and *after* crack–inclusion interaction reveal additional differences as well. The average surface roughness *Ra* was found to be consistently higher for weakly bonded inclusion specimens compared to the strongly bonded ones and the same has been demonstrated using microscopic examination of fracture surfaces.

Acknowledgements

Authors gratefully acknowledge the support for this research through a grant (NSF-CMMI-0653816) from the National Science Foundation. Financial support from US Army Research Office for the high-speed digital camera purchase through Grant DAAD19-02-10126 (DURIP) is also gratefully acknowledged.

References

[1] Tamate O. The effect of a circular inclusion on the stresses around a line crack in a sheet under tension. Int J Fract 1968;4:257–66.
[2] Evans AG. The role of inclusions in the fracture of ceramic materials. J Mater Sci 1974;9:1145–52.
[3] Erdogan F, Gupta GD, Ratwani M. Interactions between a circular inclusion and an arbitrarily oriented crack. J Appl Mech 1975;41:1007–13.
[4] Bush MB. The interaction between a crack and a particle cluster. Int J Fract 1997;88:215–32.
[5] Kitey R, Phan AV, Tippur HV, Kaplan T. Modeling of crack growth through particulate clusters in brittle matrix by symmetric-Galerkin boundary element method. Int J Fract 2006;141:11–25.
[6] Li R, Chudnovsky A. Variation of the energy release rate as a crack approaches and passes through an elastic inclusion. Int J Fract 1993;59:69–74.
[7] Li R, Chudnovsky A. Energy analysis of crack interaction with an elastic inclusion. Int J Fract 1993;63:247–61.
[8] Mantic V. Interface crack onset at a circular cylindrical inclusion under a remote transverse tension. Application of a coupled stress and energy criterion. Int J Solids Struct 2009;46:1287–304.
[9] O'Toole BJ, Santare MH. Photoelastic investigation of crack-inclusion interaction. Exp Mech 1990;30:253–7.
[10] Li R, Wu S, Ivanova E, Chudnovsky A, Sehanobish K, Bosnyak CP. Finite element model and experimental analysis of crack-inclusion interaction. J Appl Polym Sci 1993;50.
[11] Savalia PC, Tippur HV. A study of crack–inclusion interactions and matrix–inclusion debonding using Moiré interferometry and finite element method. Exp Mech 2007;47:533–47.
[12] Kitey R, Tippur HV. Dynamic crack growth past a stiff inclusion: optical investigation of inclusion eccentricity and inclusion–matrix adhesion strength. Exp Mech 2008;48:37–53.
[13] McNeill SR, Peters WH, Sutton MA. Estimation of stress intensity factor by digital image correlation. Engng Fract Mech 1987;28:101–12.
[14] Bruck HA, McNeill SR, Sutton MA, Peters WH. Digital image correlation using Newton–Raphson method of partial differential correction. Exp Mech 1989;29:261–7.
[15] Abanto-Bueno J, Lambros J. Investigation of crack growth in functionally graded materials using digital image correlation. Engng Fract Mech 2002;69:1695–711.
[16] Mekky W, Nicholson PS. The fracture toughness of Ni/Al_2O_3 laminates by digital image correlation. I: experimental crack opening displacement and *R*-curves. Engng Fract Mech 2006;73:571–82.
[17] Mogadpalli GP, Parameswaran V. Determination of stress intensity factor for cracks in orthotropic composite materials using digital image correlation. Strain 2008;44:446–52.
[18] Reu PL, Miller TJ. The application of high-speed digital image correlation. J Strain Anal Engng Des 2008;43:673–88.
[19] Kirugulige MS, Tippur HV, Denney TS. Measurement of transient deformations using digital image correlation method and high-speed photography: application to dynamic fracture. Appl Opt 2007;46:5083–96.
[20] Kirugulige MS, Tippur HV. Measurement of fracture parameters for a mixed-mode crack driven by stress waves using image correlation technique and high-speed digital photography. Strain 2009;45:108–22.
[21] Lee D, Tippur H, Kirugulige M, Bogert P. Experimental study of dynamic crack growth in unidirectional graphite/epoxy composites using digital image correlation method and high-speed photography. J Compos Mater 2009;43:2081–108.
[22] Deng X. General crack-tip fields for stationary and steadily growing interface cracks in anisotropic bimaterials. J Appl Mech 1993;60:183–9.
[23] Tippur HV, Krishnaswamy S, Rosakis AJ. Optical mapping of crack tip deformations using the methods of transmission and reflection coherent gradient sensing: a study of crack tip K-dominance. Int J Fract 1991;52:91–117.
[24] Arakawa K, Takahashi K. Relationships between fracture parameters and fracture surface roughness of brittle polymers. Int J Fract 1991;48:103–14.
[25] Sharon E, Gross SP, Fineberg J. Energy dissipation in dynamic fracture. Phys Rev Lett 1996;76:2117.